Numerical modeling of an estuary: A comprehensive skill assessment

John C. Warner

U.S. Geological Survey, Woods Hole, Massachusetts, USA

W. Rockwell Geyer

Applied Ocean Physics and Engineering, Woods Hole Oceanographic Institution, Woods Hole, Massachusetts, USA

James A. Lerczak

Department of Physical Oceanography, Woods Hole Oceanographic Institution, Woods Hole, Massachusetts, USA

[1] Numerical simulations of the Hudson River estuary using a terrain-following, three-dimensional model (Regional Ocean Modeling System (ROMS)) are compared with an extensive set of time series and spatially resolved measurements over a 43 day period with large variations in tidal forcing and river discharge. The model is particularly effective at reproducing the observed temporal variations in both the salinity and current structure, including tidal, spring neap, and river discharge–induced variability. Large observed variations in stratification between neap and spring tides are captured qualitatively and quantitatively by the model. The observed structure and variations of the longitudinal salinity gradient are also well reproduced. The most notable discrepancy between the model and the data is in the vertical salinity structure. While the surface-to-bottom salinity difference is well reproduced, the stratification in the model tends to extend all the way to the water surface, whereas the observations indicate a distinct pycnocline and a surface mixed layer. Because the southern boundary condition is located near the mouth the estuary, the salinity within the domain is particularly sensitive to the specification of salinity at the boundary. A boundary condition for the horizontal salinity gradient, based on the local value of salinity, is developed to incorporate physical processes beyond the open boundary not resolved by the model. Model results are sensitive to the specification of the bottom roughness length and vertical stability functions, insofar as they influence the intensity of vertical mixing. The results only varied slightly between different turbulence closure methods of k-ε, k-ω, and k-kl.

Citation: Warner, J. C., W. R. Geyer, and J. A. Lerczak (2005), Numerical modeling of an estuary: A comprehensive skill assessment, *J. Geophys. Res.*, *110*, C05001, doi:10.1029/2004JC002691.

1. Introduction

[2] The estuarine salinity structure is a result of the interplay between the buoyancy flux from riverine inflow, advection by tides and the estuarine circulation, and mixing. Accurate numerical predictions of the time-dependent salinity field thus depend critically on the model representation of tidal and subtidal motions as well as the subgrid-scale turbulence closure parameterizations for mixing of momentum and salt. These complex interactions at tidal and longer timescales make the evaluation of estuarine numerical models particularly challenging.

[3] A number of recent modeling studies of estuaries have considered one-dimensional (vertical) representations of the velocity and salinity fields [*Nunes Vaz et al.*, 1989; *Simpson et al.*, 1990, 1991; *Simpson and Sharples*, 1991; *Nunes Vaz and Simpson*, 1994; *Monismith and Fong*,

1996; *Zhou*, 1998] with the dual objectives of evaluating turbulence closure models and examining the interactions between tidal shears, mixing and stratification. The process of tidal straining [*Simpson et al.*, 1990], spring neap variation in stratification [*Haas*, 1977], and tidal asymmetry in mixing [*Jay and Musiak*, 1996] are amenable to one-dimensional numerical analysis if the longitudinal salinity structure can be properly specified and if lateral processes are not important. However, comparisons between these one-dimensional models and observations often indicate serious discrepancies that may in part be due to unresolved variations of the salinity gradient [*Simpson and Sharples*, 1991; *Sharples and Simpson*, 1993] or inadequacy of the turbulence closure [*Simpson and Sharples*, 1991; *Nunes Vaz and Simpson*, 1994]. One common failure of one-dimensional models with second-order closure (e.g., the MY 2.5 model [*Mellor and Yamada*, 1982]) is "runaway stratification" [*Simpson and Sharples*, 1991; *Sharples and Simpson*, 1993; *Nunes Vaz and Simpson*, 1994; *Monismith et al.*, 1996; *Stacey*, 1996] in which the stratification tends
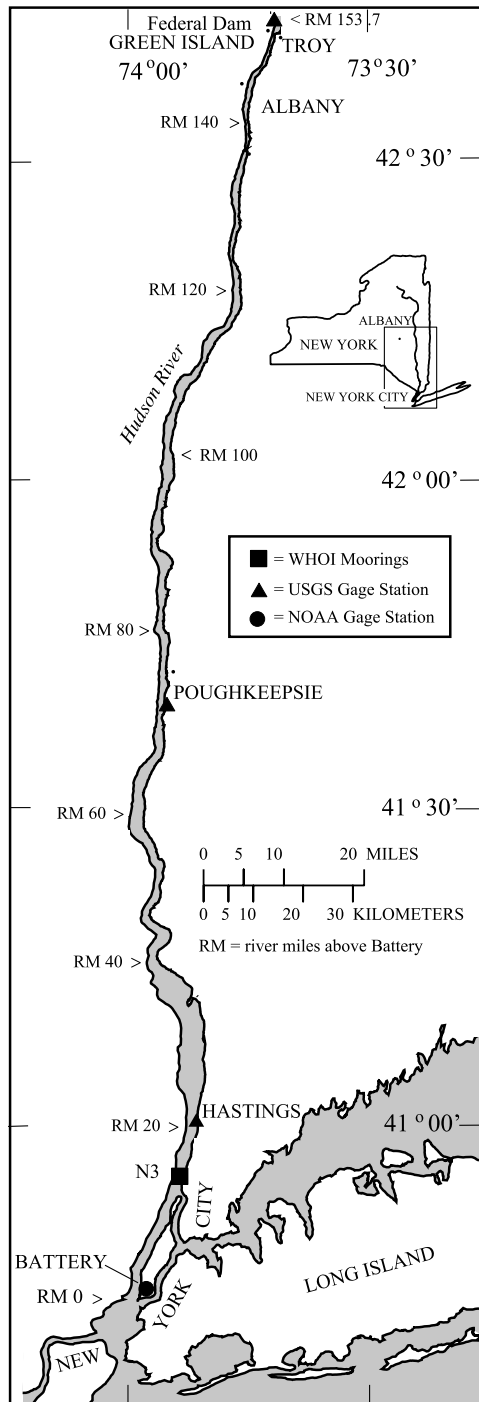
Figure 1. Hudson River, observation site locations, and model domain.

to increase without bound when the tidal amplitude drops below some threshold value. This behavior may indicate a failure of the closure or it may relate to inadequate constraints on the salinity gradient in the one-dimensional formulation.

[4] Classical estuarine theory by *Hansen and Rattray* [1965] and *Chatwin* [1976] demonstrate that the longitudinal salinity gradient ($\partial s/\partial x$) is not an independent variable, but rather it is part of the solution of the momentum and salinity conservation equations for a specified freshwater

outflow. Although the *Hansen and Rattray* [1965] solution assumes that the salinity gradient has no vertical variation, the Chatwin solution requires that the gradient vary vertically in order to satisfy the global salt balance. The analysis by *Kranenburg* [1986] demonstrates the large temporal variability of $\partial s/\partial x$ due to variations in runoff. Similarly, *MacCready* [1999] and *Hetland and Geyer* [2005] use numerical models to indicate the variations of $\partial s/\partial x$ with tidal amplitude. These theoretical and idealized numerical studies suggest that the salinity gradient should be included as a dependent variable in the problem, thus limiting the prognostic ability of one-dimensional (vertically resolving) models.

[5] The problem of specifying the salinity gradient can be overcome with three-dimensional simulations, wherein the longitudinal salinity gradient becomes a dependent variable. There have been few applications of three-dimensional models of estuaries in which the variability of the stratification, tidal and mean shear, and longitudinal salinity gradient have been evaluated. *Prandle* [2004, p. 385] notes that model applications to date have shown "limited agreement...between observation and model results for the sensitivity of saline intrusion to tidal range (spring to neap) and river flow." *North et al.* [2004] found it necessary to tune a Richardson number–dependent vertical mixing parameterization to realistically model a salt front structure. They conclude that better parameterizations of turbulence in stratified flows are crucial for understanding and modeling estuarine circulation. *Stenström* [2004] simulated a reach of the Hudson River estuary for a neap semidiurnal tidal cycle. Model results compared well with observations for that limited time period but he also states that future studies are needed to further develop and evaluate the closure schemes. Recently M. Li et al. (Simulation of Chesapeake Bay estuary: Sensitivity to turbulence mixing parameterizations and comparison with hydrographic observations, submitted to *Journal of Geophysical Research*, 2004) have demonstrated strong consistencies in results from several turbulence closure models and conclude that the models perform well in the bottom boundary layer mixing, but perform poorly in the stratified pycnocline region, where the models have a strong dependence on background mixing values. Discrepancies between model results and observations may be the result of inadequacies of the closure scheme, inaccurate or unresolved forcing data, or inadequate grid resolution. In any case, three-dimensional models need more rigorous testing against estuarine data sets to assess model performance.

[6] This paper provides a comparison of a three-dimensional model simulation to an extensive set of time series and spatially resolved measurements of the Hudson River estuary. The measurements extend over a 43 day period, with several spring neap cycles of tidal amplitude variation and large variations in river discharge associated with the spring freshet. The measurements included a number of realizations of the along-estuary salinity distribution as well as time series data at various vertical and cross-estuary locations. These measurements provide an excellent test of the model's ability to reproduce the variations in stratification on both tidal and subtidal timescales, as well as the longitudinal salinity gradient and length of salt intrusion through a broad range of forcing conditions.
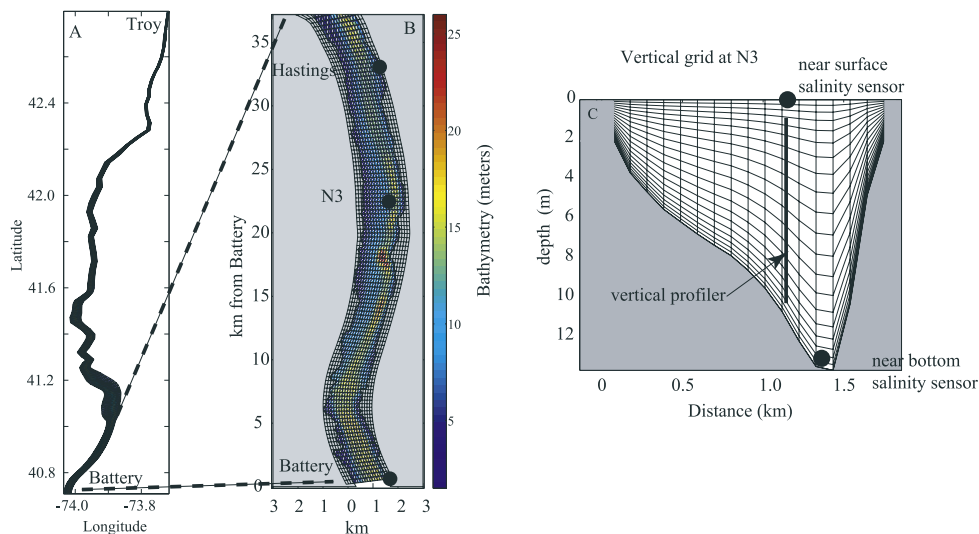
Figure 2. Numerical model grid showing (a) a full horizontal orthogonal curvilinear grid of 20×200 cells, (b) a closeup of bathymetry and grid for lower 35 km (main focus area), and (c) vertical stretched terrain following coordinates for the cross section at site N3.

[7] In section 2 we discuss the observational data collection program and numerical model. Results of the numerical simulations and comparison to the observational data are presented in section 3. Section 4 provides an assessment of the sensitivity of the model to turbulence closure parameters and unresolved forcing variables. Section 5 is a discussion and the summary and conclusions are found in section 6.

2. Methods

2.1. Site Description

[8] The Hudson River is located along the northeast coast of the U.S. (Figure 1) and is one of New York State's major water resources. The tidal reach of the river extends nearly 250 km north from the Battery to the Federal Dam at Troy, New York. These locations also identify the limits of our study area. The landward extent of salt can reach up to 140 km or as little as 30 km north of the Battery depending on fresh water discharge, with a typical value of 80 km [*Abood*, 1974; *Wells and Young*, 1992; *de Vries and Weiss*, 2001]. Peak to trough tidal range is on the order of 2 m and depth-mean tidal velocities reach 1 ms^{-1} during spring tides. Fresh water inflow is predominately from the upper Hudson River (above the dam) with mean summer (low flow) conditions approaching 200 m^3 s^{-1} and maximum peak seasonal releases on the order of 2000 m^3 s^{-1}.

2.2. Measurement Program

[9] A measurement program consisted of a 43 day deployment of oceanographic equipment from 23 April to 5 June 2002 (year days 113–156) (J. A. Lerczak et al., Mechanisms driving the time-dependent salt flux in a partially stratified estuary, submitted to *Journal of Physical Oceanography*, 2004, hereinafter referred to as Lerczak et al., submitted manuscript, 2004). Instruments were positioned on bottom-mounted tripods and taught wire mooring arrays at six locations at cross section N3, near river km 23 (Figure 2). Equipment consisted of sensors to measure pressure, temperature, conductivity, and vertical profiles of

velocity. An autonomous profiler was positioned slightly west of the main channel to measure vertical profiles of conductivity and temperature once per hour for 16 days (from 140 to 156).

[10] The shape of the channel cross section at this location is characterized by a shallow western side and a main channel on the east side, with a mean depth of about 15 m. Data from the instruments located in and near the channel identified in Figure 2 will be emphasized in this paper. However data from all the sites (Lerczak et al., submitted manuscript, 2004) were used to calculate cross sectional averaged quantities that are compared to model predictions. In addition, nine along-channel hydrographic surveys were carried out to measure the vertical structure of salinity along the main axis of the estuary. Typical sections started at the Battery and continued up river to the head of salt. Several surveys were limited in their coverage.

[11] Additional data sources include time series of observed sea level at the Battery from the NOAA Center for Operational Oceanographic Products and Services, available online at http://co-ops.nos.noaa.gov, station 8518750. Additional water level data at Hastings (station 01376304) and water level for Poughkeepsie (station 01372058) is from http://ny.usgs.gov/projects/poused/index.html. River discharge from the dam at Green Island was obtained from the USGS stream gage # 01358000 (http://ny.water.usgs.gov/projects/dialer_plots/saltfront.html).

2.3. Numerical Model Description

[12] The three-dimensional model used in this study is the Regional Ocean Modeling System (ROMS) v2.0 [*Haidvogel et al.*, 2000; *Shchepetkin and McWilliams*, 2005]. ROMS is a hydrostatic, primitive equation ocean model that solves the Reynolds averaged form of the Navier Stokes equations on a horizontal orthogonal curvilinear Arakawa "C" grid and uses stretched terrain following coordinates in the vertical. The model can be configured with choices from several advection schemes, pressure-gradient algorithms, turbulence closures, and types of boundary conditions. We
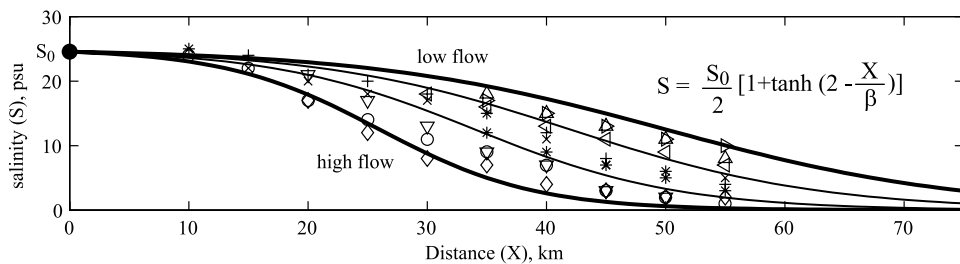
Figure 3. Observed near-bottom longitudinal salinity distribution. Symbols denote near-bottom salinity from separate along-channel hydrographic surveys. Data follow a hyperbolic tangent relation with $\beta = 26.0 - 0.01 * Q_7$.

specify a third-order upstream velocity-dependent hyper-diffusive advective scheme for the horizontal scalar and momentum transport, a spline advection scheme for vertical transport, and a Jacobian density gradient algorithm for the pressure term [*Ezer et al.*, 2002; *Shchepetkin and McWilliams*, 2003]. The simulation presented here was performed on a four processor unix-based system with Open MP directives. About 8 hours (real time) were required to complete the 50 day simulation with a grid configuration of $20 \times 200 \times 20$ cells.

[13] The model domain of the Hudson River estuary extends from the Battery to the Federal Dam (Figure 2a) and is about 250 km long. The average width in the lower reach is about 2 km, broadens to nearly 5 km north of Hastings, and then narrows to nearly 500 m near the dam. This domain is horizontally discretized with 200 along-channel and 20 cross-channel cells. Grid resolution is increased in the region of salt intrusion (first 40 km) with along-channel cell spacing on the order of approximately 300 m and lateral spacing approximately 100 m (Figure 2b). From km 40 to 250 the grid spacing telescopes linearly to reduce resolution in the upstream fresh water zone. Grid spacing approaches 4 km in length at the northern boundary. In the vertical the bathymetry varies from 2 to 25 m with a mean depth of 8 m. The vertical dimension is discretized with twenty terrain-following sigma levels (Figure 2c) and a vertical stretching parameter allows increased resolution near the surface and bottom boundaries.

[14] The momentum boundary condition on the surface is zero stress (no wind). Parameterization of the bottom stress is based on a logarithmic velocity profile with a roughness length $z_0 = 0.002$ m. This value is consistent with *Geyer et al.* [2000] where they estimated $C_d = 0.0031$ at $z = 3.5$ mab, which equates to our z_0 using the drag relation of $C_d = (\kappa/\ln (z/z_0))^2$ in a quadratic stress law. Lateral boundaries have free slip conditions.

[15] The northern momentum boundary condition is imposed on the depth-averaged velocity equated to the river discharge divided by the upstream cross-sectional area. The model domain was specifically extended north-ward to the Federal Dam to provide this simple but explicit boundary of unidirectional seaward transport with a salinity of zero. The magnitude of river discharge was multiplied by 1.4 to account for adjacent watershed areas and lateral inflow of tributaries along the length of the river. This factor is midrange between the long-term flow yield factor of 1.225 as suggested by *Abood* [1974] and the factor of 1.6 used by Lerczak et al. (submitted

manuscript, 2004) that provides a high correlation to the low-frequency (period > 5 day) measured fresh water flux at a mid estuary location. The simulated flow will there-fore be too large immediately below the dam but the magnitude of this error will decrease downstream.

[16] At the southern boundary, the model utilizes a depth-averaged momentum balance that neglects the convective acceleration and Coriolis terms. This results in a balance between the temporal acceleration with the pressure gradi-ent and bottom friction terms, satisfying the dominant along-channel momentum balance for the up-estuary prop-agating barotropic tide. The observed time series of free surface displacement at the Battery is used to drive the along-channel barotropic pressure gradient on the open boundary. Radiation boundary conditions were prescribed for the free surface and baroclinic (three-dimensional) momentum.

[17] Specification of salinity across the southern open boundary was particularly challenging, due to the lack of direct measurements, its marked tidal variability, and its dependence on the freshwater flow. Physical processes outside of the model domain and storage of fresh water in New York Harbor are not resolved by the model but affect the magnitude of salinity along the southern open boundary. To derive a boundary condition for salinity, we found that an effective approach was to impose a salinity gradient condition based on the current value of salinity at the open boundary. To derive this gradient condition, the longitudinal distribution of salt is first approximated with a hyperbolic tangent function as

$$S(X) = \frac{S_0}{2} \left[1 + \tanh\left(\alpha - \frac{X}{\beta(t)}\right) \right], \qquad (1)$$

where $S(X)$ is the longitudinal value of salinity, S_0 is the maximum value at the oceanic end, X is the longitudinal coordinate along the length of the estuary in kilometers, t is time, β is a length scale (km) for the salt intrusion, and α is a nondimensional parameter that establishes the location of the origin, chosen as $\alpha = 2$. The hyperbolic function is a well behaved relation with continuous derivatives and zero gradients at both limits. For each along-channel hydro-graphic survey, equation (1) was fit to the observed salt field by holding $S_0 = 25$ and determining best fit values of β. Results are shown in Figure 3, where each symbol represents observed near-bottom salinity values during the nine long-itudinal channel surveys. The parameter β accounts for changes in salt intrusion length, with variability due

predominately from changes in river flow. Best fit β values were regressed against 7 day lagged, 7 day mean discharge (Q_7) resulting with $\beta = 26 - 0.01\,Q_7$, with an $r^2 = 0.71$ and is statistically significant ($p = 0.004$). These average and lag timescales are in agreement with *Abood* [1974, p. 88] who finds that the salinity lags the flow by 5–10 days. The variation of β indicates a contraction of the salt intrusion with increase of river flow. For the study period, Q_7 varied from order 500 to 1500 $m^3\ s^{-1}$ resulting in variations of β from 21 to 11 km, equating to a 50% reduction of the salt intrusion due to the freshet.

[18] The horizontal salinity gradient ($\partial s / \partial x$) for the open boundary is obtained from the derivative of equation (1) with respect to X as

$$\partial s / \partial x = -\frac{S_0}{2\beta} \operatorname{sech}^2 \left(\alpha - \frac{X}{\beta} \right). \qquad (2)$$

The gradient condition is then applied at the estuary mouth. Physically, as the river flow increases the local salinity gradient at the mouth must increase to compensate for the decrease in salt intrusion length. Numerically the parameter β provides the feedback to the boundary salinity gradient for changes in river flow.

[19] Equation (2) can be expressed in terms of the salinity at the first interior point ($s_1(y, z, t)$) after substitution of X from equation (1), to yield

$$\frac{\partial s}{\partial x}(y,z,t) = -\frac{S_0}{2\beta} \operatorname{sech}^2 \left(\tanh^{-1} \left(\frac{2\,s_1}{S_0} - 1 \right) \right). \qquad (3)$$

The boundary value of salinity is derived from equation (3), imposed for all vertical levels at the open boundary as

$$s_0 = s_1 - \partial s / \partial x * \Delta x, \qquad (4)$$

where s_0 is the salinity along the open boundary and Δx is the local along-channel cell spacing. As the magnitude of salinity approaches zero or S_0 the horizontal salinity gradient (equation (3)) approaches zero. Midrange salinity values yield gradients on the order of 0.5 psu/km for low river discharge conditions and approach 0.9 psu/km for high river discharge. Theses values of $\partial s / \partial x$ are consistent with observed gradients [*Geyer et al.*, 2000].

[20] Parameterizations for subgrid-scale mixing of mass and momentum are determined using the Generic Length Scale turbulence closure method (GLS [*Umlauf and Burchard*, 2003]). The GLS method is a two-equation model with one equation for the transport of turbulence kinetic energy and a second equation for the transport of the length scale–related parameter. Specific implementation of this method is discussed in detail by *Warner et al.* [2005]. In this paper we use the GLS method as a tool that simplifies the numerical implementation and allows exact recovery of the two equation models of k-kl, k-ε, and k-ω. Three simulations were performed, identical in all aspects, except for the turbulence closure. The first simulation uses the k-kl model, which is a modified form of the Mellor/ Yamada Level 2.5 closure [*Mellor and Yamada*, 1982]. Modifications include the correct value for the buoyancy term [*Burchard*, 2001], consistent length scale limitation,

and the wall function for open channel flows [*Blumberg et al.*, 1992]. The second simulation uses the k-ε closure [*Rodi*, 1984] with buoyancy parameters as discussed by *Burchard et al.* [1998] and *Burchard and Bolding* [2001]. The third simulation uses the k-ω model [*Wilcox*, 1988] and has been widely used in boundary layer modeling [*Wilcox*, 1998] with a recent extension for application to buoyancy affected flows [*Umlauf et al.*, 2003]. Parameter values for the buoyancy flux term in all three methods were derived based upon a steady state Richardson number criteria and validated with a surface wind mixing experiment [*Burchard et al.*, 1998; *Warner et al.*, 2005]. Unless stated otherwise, results presented throughout the manuscript are from simulations using the k-ω closure and the *Kantha and Clayson* [1994] (hereinafter referred to as KC) stability functions for closure of the second moments. Minimum values of vertical eddy viscosity and diffusivity were set equal to $5 \times 10^{-6}\ m^2\ s^{-1}$.

[21] The model was initiated from rest with a stratified salinity field along the lower 50 km of the estuary. Initial bottom salinity values range from 25 psu at the mouth to 0 psu at 50 km, with stratification of 10 psu at the mouth and 0 at the limit of salt intrusion. These values simulate a typical salt intrusion during the simulation period. Hydrodynamic conditions of the estuary were simulated for 50 days, however, the first 10 days provide dynamic adjustment of the density field from initial conditions and are not used in the analysis. Because the domain is strongly advection dominated, and based upon numerous simulations, the time period of 10 days is sufficient for the results to become insensitive to the initial conditions, an adjustment timescale consistent with *Abood* [1974]. Results are presented for days 110–150.

2.4. Model Skill

[22] Predictive skill is based on quantitative agreement between model and observations. Using a method presented by *Wilmott* [1981] we define

$$\text{Skill} = 1 - \frac{\sum |X_{\text{model}} - X_{\text{obs}}|^2}{\sum \left(|X_{\text{model}} - \overline{X_{\text{obs}}}| + |X_{\text{obs}} - \overline{X_{\text{obs}}}| \right)^2}, \qquad (5)$$

where X is the variable being compared with a time mean $\overline{X}$. Perfect agreement between model results and observations will yield a skill of one and complete disagreement yields a skill of zero. Model skill is evaluated for all prognostic quantities.

3. Results

3.1. Sea Level

[23] The semidiurnal tidal components of the M2, N2, S2, O1, and K1 explain 92% of the sea level variance, with the remaining variations caused by tidal interactions and lower-frequency tidal and meteorological forcings. At the Battery (Figure 4a) there is identical agreement between the model and observed free surface because the model is forced with this time series ("skill" = 1.0). As one travels upstream the model skill at Hastings and Poughkeepsie (Figures 4b and 4c) remains high with values of 0.95 and 0.85, respectively. Differences in phase between the model and
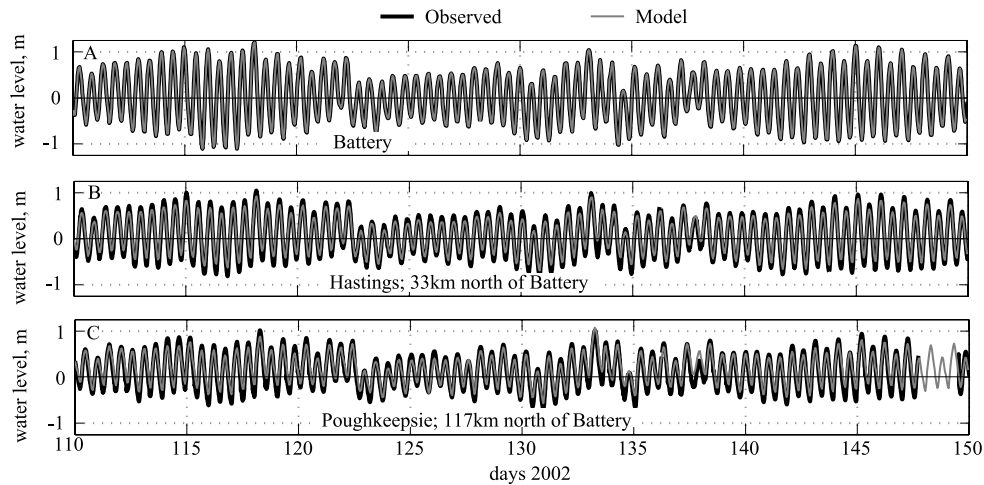
Figure 4. Comparison of observed and modeled time series of free surface at site (a) Battery (southern boundary condition), (b) Hastings, and (c) Poughkeepsie.

the observations are minimal, with a maximum difference in the M2 component of 3 degrees at Hastings (not shown). Differences in the M2 amplitude between the model and observations are more significant, with a maximum error of 10% in the lower part of the domain and increasing to nearly 15% in the northern part of the domain, beyond the region of salt intrusion. The barotropic pressure gradient between the Battery and Hastings has a skill of 0.93 and decreases to 0.85 between Hastings and Poughkeepsie. These differences in the sea level are not significantly reduced by changing the bottom drag coefficient, and it is not clear why they occur. The sea level differences may be a result of the low grid resolution in the upper portion of the model domain. However, because the main objective of this study was to model the region of salt intrusion of the estuary, the errors in the upstream water levels were not investigated further.

3.2. Velocity

[24] Similar to the sea level, along-channel velocity is dominated by the semidiurnal tide and exhibits a spring neap variation. Figure 5 compares time series of observed and modeled depth-averaged velocity at site N3 in the channel. The model skill is 0.92. Depth-averaged magnitudes of velocity approach 1.0 ms^{-1} during spring tides, and reduce to nearly 0.50 ms^{-1} during neap tides.

3.3. Salinity

[25] The 50 day simulation period includes three spring tides and two neap tides. Spring tides are centered on days 117, 132, and 145 (Figure 6a). The magnitude of

semidiurnal tidal sea level amplitude approaches 0.8 m during spring tides and decreases to nearly 0.40 m during neap tides. River discharge (Figure 6a) imposed at the landward boundary varied from a flow of $400 \text{ m}^3 \text{ s}^{-1}$ to a freshet that reached $2400 \text{ m}^3 \text{ s}^{-1}$ from days 132–140. The increased fresh water transport was coincident with the weakest of the spring tides.

[26] The model has a skill of 0.85 in simulating the observed time series of surface and bottom salinity at N3 (Figure 6b). This high skill is due in part to the models ability to effectively simulate the large amplitude low-frequency variations in salinity caused by changes in river flow and spring neap variations in mixing. In addition, the model effectively simulated the tidal high-frequency variations in salinity. Skill is similar at 0.85 for just the tidal variations (low frequency removed). Variations in salinity due to tidal advection of the along-channel salinity gradient are about 5–10 psu during spring tides and 1–3 psu during neap tides. On a fortnightly timescale, both the onset and magnitude of stratification are captured by the model (Figure 6b). Stratification is weakest during spring tides and strongest during neap tides. Spring tides produce increased turbulence, which increases mixing and leads to a nearly well-mixed water column. Spring tides centered on days 117 and 145 produce nearly vertical isohalines with nearly equal near bottom and surface values of salinity (Figure 6c). Neap tidal periods, conversely, show the development of strong stratification. In ~15 m water depth, the difference of surface to bottom salinity varies from near 0 psu during spring tides to over 20 psu during neap tides. Variations in river flow cause large variations in salinity as
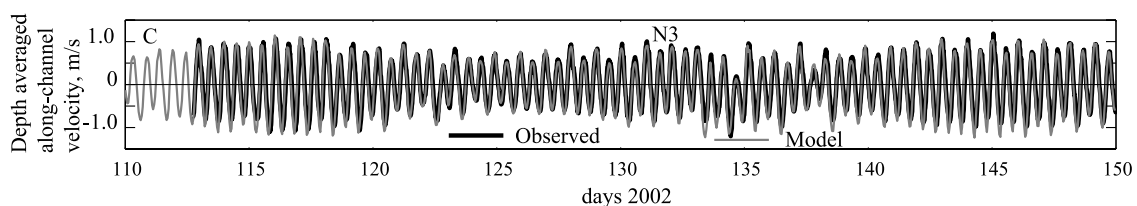

Figure 5. Comparison of observed and modeled depth-averaged velocity in the channel at N3.
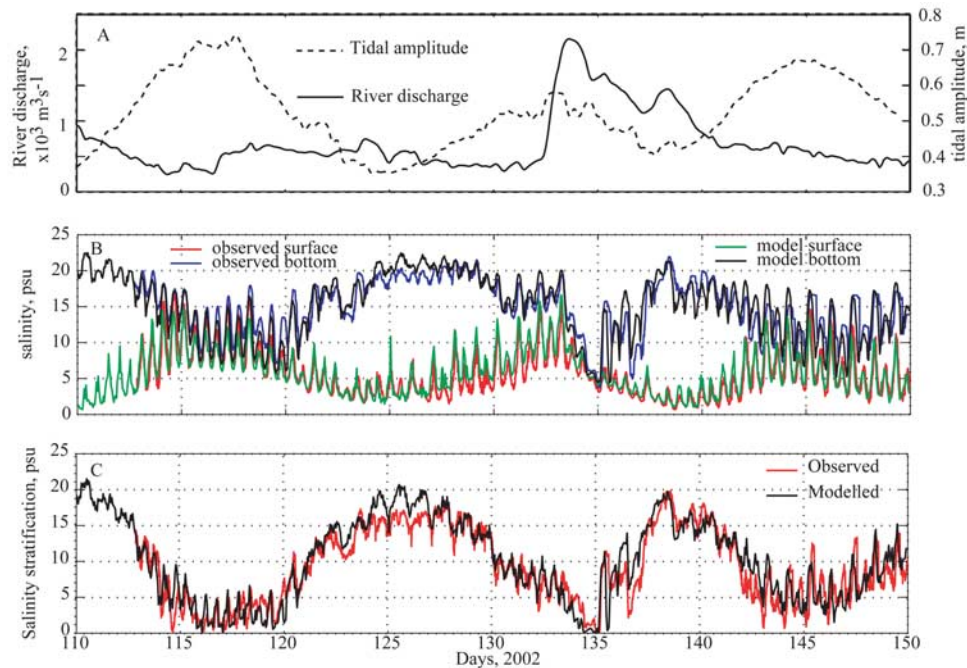
Figure 6. (a) Environmental conditions of river discharge at Green Island Dam and amplitude of semidiurnal sea level. Comparison of observational and model results at site N3 for (b) surface and bottom salinity and (c) vertical salinity stratification.

well as stratification. The strong river discharge near day 133 displaces the limit of the salt intrusion seaward and decreases the salinity to nearly 5 psu in the channel at N3, with an accompanying reduction in stratification. The model is consistent with the observations for both timing and magnitude of salinity variations in the response to this high-flow event.

3.4. Vertical Structure

[27] Figure 7 shows phase averages for the vertical structure of velocity and salinity at site N3 from a location slightly west of the main channel in ~10 m of water where the vertically profiling instrument package was deployed. Vertical profiles of velocity and salinity are computed for tidal phases of maximum ebb and flood and averaged for neap (Figures 7a and 7c) and spring (Figures 7b and 7d) tidal conditions. Concurrent modeling and observational data from the profiler provided approximately five time periods for each phase average, between days 140 and 150. The ebb profiles of velocity exhibit strong shear during both neap and spring tidal conditions and observations and model results are in close agreement at these times. Flood tidal currents during neap tides (Figure 7a) exhibit a subsurface maximum as is characteristic of highly stratified estuaries [*Geyer and Farmer*, 1989], and indicates that the bottom boundary layer does not reach the surface. Model simulations also show a subsurface maximum. However, instantaneous profiles often do not reach as high in the water column as observed and the phase-averaged profiles exhibit a weaker subsurface maximum. During spring flood tides the observations show an increasing shear profile up to the water surface, indicating that the boundary layer extends to the free surface (Figure 7b). The model, however, still

exhibits a slight subsurface maximum, indicating that the model is underestimating the vertical growth rate of the boundary layer. Mean predictive skill for these vertical velocity profiles is 0.89 (using equation (5) with a vertical mean).

[28] The observed vertical structure of salinity during neap tides (Figure 7c) consists of a well-mixed bottom boundary layer, a zone of strong stratification, and a surface layer. Model results typically demonstrate equivalent top-bottom salinity difference (Figure 6c), but the vertical structure differs from that of the observations. The model does not show a distinct inflection point in the salinity profile, as is evident in the observations.

[29] During spring tides the stratification is greatly reduced (Figure 7d). Observations show a constant increase of stratification during both the ebb and flood. The model predicts nearly equivalent levels of stratification as observed, with a slightly displaced mean value. Mean predictive skill for these vertical salinity profiles is 0.77.

[30] Figure 7 also provides a comparison of the performance of the three different turbulence closure parameterizations: k-ω, k-kl, and k-ε. All three methods yield similar results with respect to tidal shear and vertical stratification of salt. Of the three models, results from the k-ε and k-ω are most similar with k-kl exhibiting slightly larger shear and slightly greater stratification. While simulations using the different turbulence closures are similar, slight variations in the simulations exist. Typical maximum variations in magnitude of salinity between the closures are on the order of 15%, with more variance in the prediction of salinity than velocity. More directed field measurements are required to successfully evaluate the performance of these closure models, but the comparison demonstrates the need for
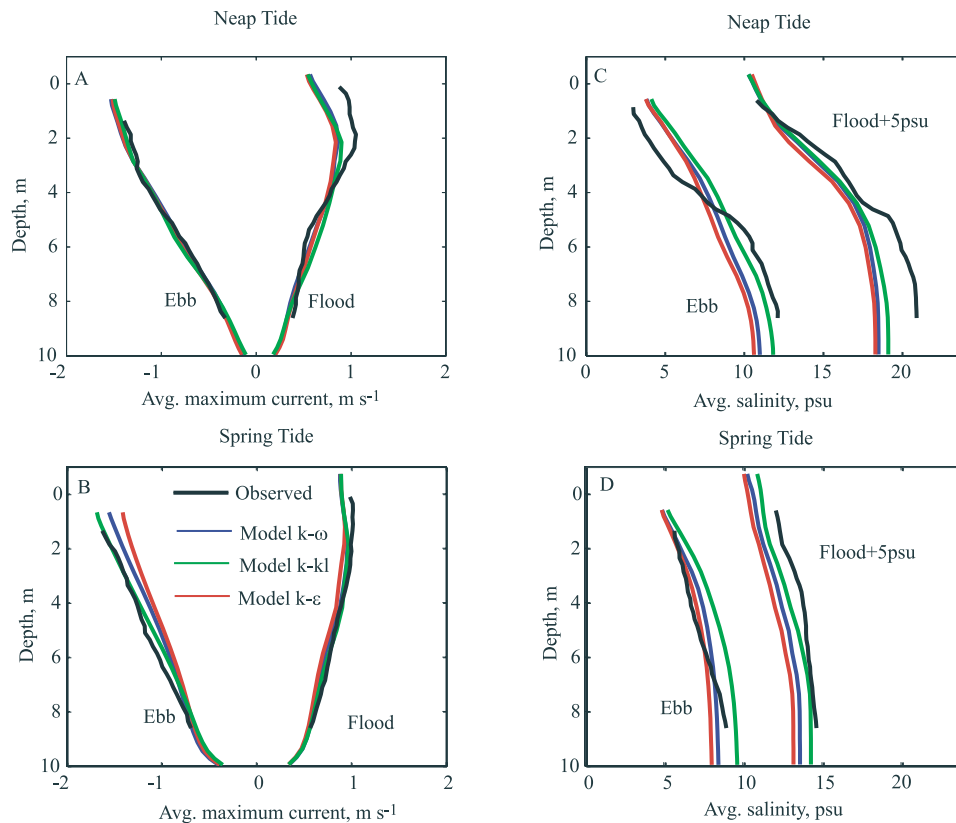
Figure 7. Vertical structure of modeled and observed tidal currents and salinity at site N3. Average maximum flood and maximum ebb tidal current profiles during (a) neap tides and (b) spring tides. Average salinity profiles at maximum flood and maximum ebb during (c) neap tides and (d) spring tides. Flood tide salinity profiles are offset 5 psu.

improvement of the parameterization of the vertical structure of turbulence.

3.5. Longitudinal Structure

[31] A pronounced difference in the longitudinal structure of the salinity intrusion is apparent between neap and spring tides. Figure 8 compares along-channel hydrographic surveys to model results for a neap tide (Figures 8a and 8b, day 140.56, approaching max ebb) and a spring tide (Figures 8c and 8d, day 145.59, increasing flood current). Observational casts were advected using the tidal currents to a single time instance to produce quasi-synoptic sections for comparison to instantaneous model simulations. This transformation affects the horizontal gradients but it does not alter the qualitative features of the data. Comparisons to nonadvected casts provide similar comparisons.

[32] During neap tides (Figure 8a) strong stratification is observed to extend from the Battery to the limit of salt intrusion. From km 0 to near km 30 a well-mixed bottom boundary layer is separated from the surface mixed layer by a region of strong halocline. The halocline extends vertically from approximately 3 to 7 m deep. From km 30 to the limit of salt intrusion near km 50 the water column is still stratified but does not show a strong middepth halocline. The model during neap tides (Figure 8b) has a sharp halocline near the mouth from km 0 to near 25, as observed in the data. However, further landward from km 25 to near 50 the model stratification is more uniform with depth.

The model is predicting the correct top-to-bottom salinity difference, but the vertical structure is more diffusive than the observations (as is also shown in Figure 7c).

[33] During spring tides the observed salinity field (Figure 8c) is weakly stratified, and the isohalines tend to a vertical orientation throughout the domain. The length of the salt intrusion is slightly less than during the neap tide, with the 1 psu isohaline extending to km 43. The time of this survey is during a weak flood tide. The simulated salinity intrusion, during the same period as the observed spring tide section, has a slightly reduced level of stratification compared to the observations.

3.6. Longitudinal Salinity Gradient

[34] In this context the salt intrusion length is defined by the landward location of the 5 psu isohaline, chosen to allow comparison with longitudinal surveys that did not always reach the head of salt. The model salt intrusion length (Figure 9) varies both on the tidal timescale and with lower frequency oscillations due to variations in river flow and spring/neap variations in tidal mixing. On a semidiurnal timescale, the salt front advects landward and seaward on the order of 7 km during spring tides and 3 km during neap tides. At lower frequencies, the salt front is displaced on the order of 20 km. The salinity intrusion advances landward during neap tides when estuarine circulation is strongest. Maximum landward intrusion occurs after the time of minimal tidal energy
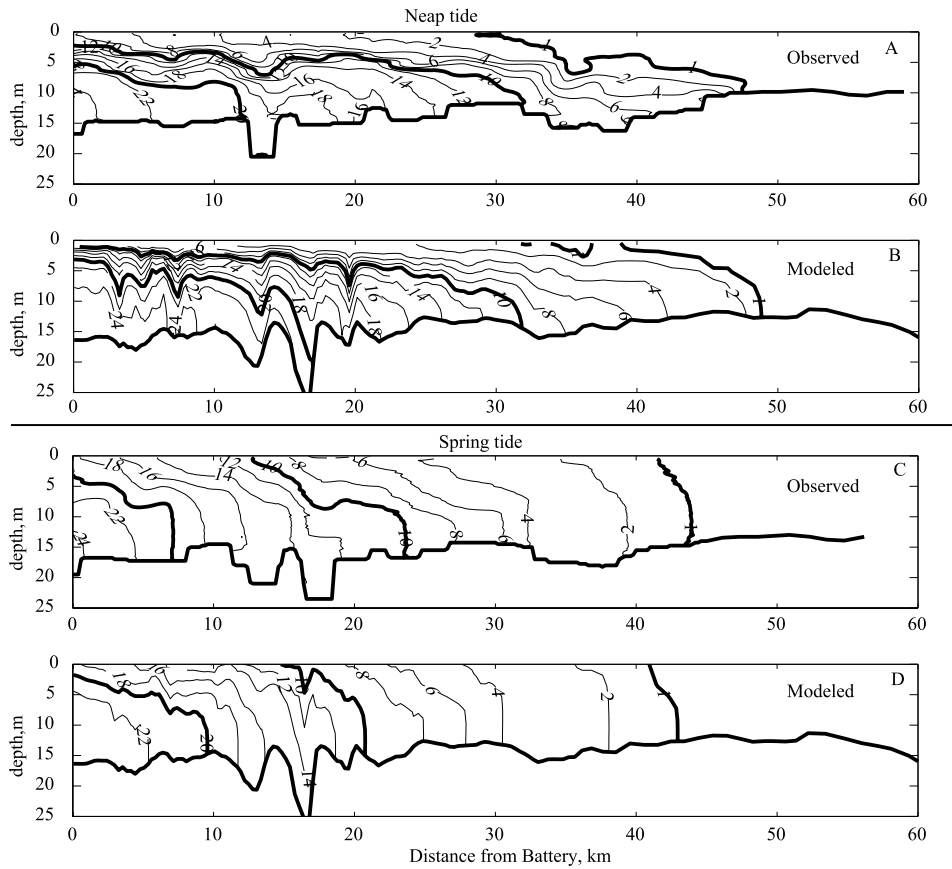
Figure 8. Comparison of longitudinal salinity distribution during neap tide (day 140.56) for (a) observed and (b) modeled and during spring tide (day 145.59) for (c) observed and (d) modeled.

and is approximately in quadrature with the spring neap cycle in tidal amplitude (Figure 6a), suggesting that the "velocity" of the salt front is approximately in phase with the tidal amplitude (except with a different sign). Figure 9 shows maximum landward intrusion on days 113 and 128, corresponding to a 3–4 day lag after the neap tides on days 110 and 124.

[35] River discharge significantly affects the salt intrusion length. The peak flow event during this study on day 134 displaced the salt intrusion seaward to near km 21, consistent with *Abood* [1974, Figure 21]. Observed limits of salt intrusion (Figure 9) are consistent with the model simulations. Only a limited number of observations were available

for this assessment, but they allow a comparison during both spring and neap tidal conditions. Model skill for salt intrusion length is 0.87.

[36] Estimates of near-surface horizontal salinity gradient (Figure 10) were computed from point values of salinity between Hastings and N3. These values provide the longest time series of available data. The gradient was computed on a tidal timescale and then low-pass filtered to remove tidal effects, and varies between 0.2 and 0.9 psu km^{-1}. The reduced gradient near day 134 is due to the large river flow that pushed the salinity gradient seaward of this part of the river. The model skill is 0.82. The model is effective at capturing the large amplitude variability but deviates in
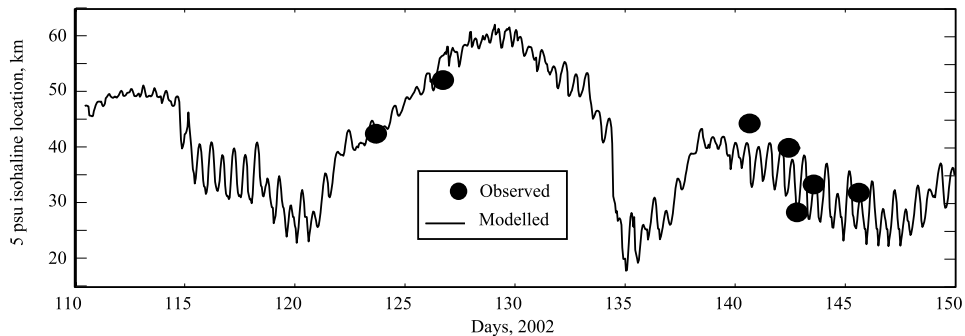

Figure 9. Limit of salt intrusion calculated as the landward extent of 5 psu isohaline.
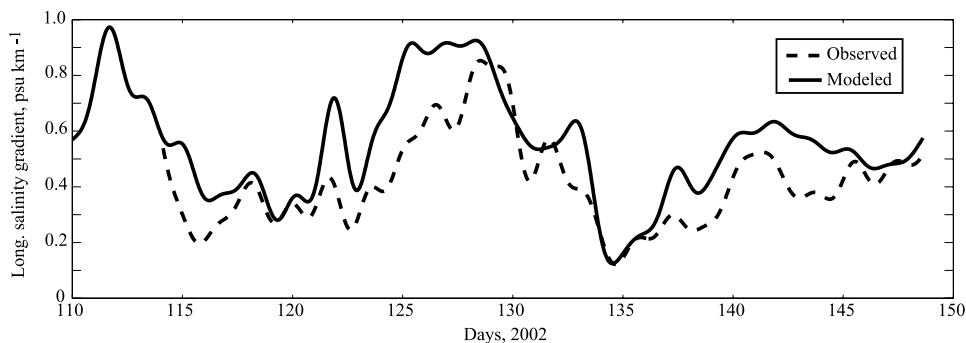
Figure 10. Comparison of observed and modeled longitudinal salinity gradient from Hastings to N3.

magnitude from the observed, especially near day 125 during a neap tide.

3.7. Salt Flux

[37] Estuarine circulation, tidally averaged transport, and salt flux are fundamental quantities that characterize an estuary. Estuarine circulation is calculated as

$$u_{est} = u - \langle u \rangle, \qquad (6)$$

where u_{est} is the estuarine circulation, u is the depth-varying velocity and $\langle u \rangle$ is the depth-averaged velocity. A comparison of observed to modeled tidally averaged estuarine circulation is shown in Figure 11. The estuarine circulation at 2.2 mab maintains a nearly consistent landward magnitude slightly less than 0.2 ms^{-1}, with slightly decreasing magnitude during spring tides. The surface return flow shows greater variability and fluctuates between -0.1 and -0.5 ms^{-1}. Surface variability is more coherent with low-frequency weather signals. The magnitude of the circulation is consistent with previous observations [*Bowen and Geyer*, 2003]. The model skill is 0.78 for the 2.2 mab and 0.68 for the 13.5 mab. Greatest deviations between model and observed occur at the 13.5 mab level, especially near day 125 during the neap tide. At this time the model is overpredicting the surface-bottom salinity difference (see Figure 6c at day 125) and the increased stratification is decoupling the surface flow providing greater seaward transport.

[38] The model has a predictive skill of 0.91 for the tidally averaged transport (mass flux of water). Calculations

from the model and observations are based on the low-pass filter of cross-sectional average total transport (Figure 12a). A strong subtidal 5 day period is predominant in the early part of the record, most likely due to atmospheric induced perturbations propagating into the domain. The model captures these oscillations effectively because it is forced with the observed free surface displacement. The large river discharge near day 134 is also captured in both magnitude and phase by the model, demonstrating a correct travel time of freshwater flow through the domain.

[39] Salt flux (Figure 12b) is calculated for the cross section to predict total scalar transport. The horizontal salt flux is the cross-sectionally integrated product of salinity and along-channel velocity. Predictive skill is similar to that for total transport. During the early part of the record the flux fluctuates with similar 5 day period as for the mass transport of water. Salt flux is into the estuary during neap tides and out of the estuary during spring tides. The peak in river flow generated the largest out-estuary salt flux near day 134. The greatest variation between the model and observed occurred near day 125 during a neap tide. The variation is most likely reflecting that the model overestimated the top-bottom salinity difference, as described for the estuarine circulation. At this time (see Figure 6c at day 125) and therefore overpredicting the landward salt flux.

4. Model Sensitivity

[40] Sensitivity analysis of the model indicate that the most important variables affecting the simulation of velocity and salinity are variations to the bottom drag coefficient, the
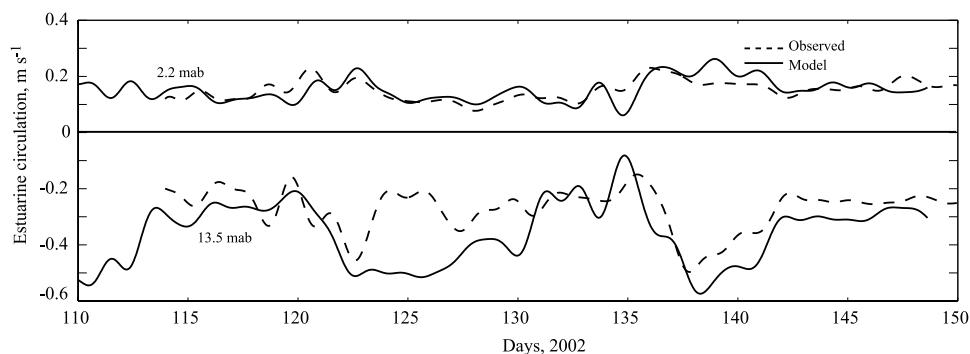

Figure 11. Estuarine circulation at depths of 2.2 and 13.5 meters above bottom (mab). Positive values are landward flow, negative seaward.
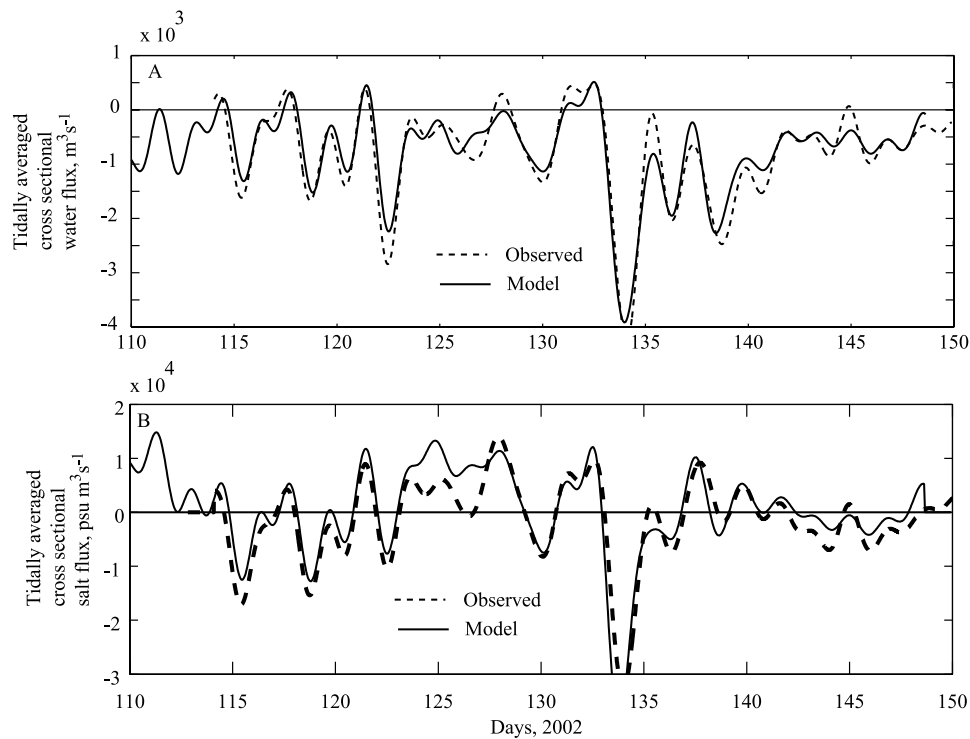
Figure 12. Comparison of observed and modeled cross-sectional average (a) water and (b) salt flux.

salinity condition at the southern open boundary, and the stability functions for the turbulence closures. The bottom stress in the study area has previously been established based on observational analysis of the momentum balance [*Geyer et al.*, 2000] and we chose to use this value in the model. Decreasing the roughness length an order of magnitude below our specified value to $z_0 = 0.0002$ led to slightly increased near bottom velocities and reduced vertical migration of the bottom boundary layer up into the water column. These factors result in reduced mixing and increased intrusion of salt on the order of 10 km beyond the observations.

[41] Variations to the southern boundary condition provided insight to the significance of the salinity at this boundary. A simulation that held this value to a constant $s_0 = 25$ (s_0 in equation (4), i.e., neglecting dependence on river flow) resulted in an overestimate of the salt intrusion length, although the magnitude of top-bottom salinity difference and vertical structure of salinity are still consistent with previous simulations. The constant boundary condition effectively displaced the salt field landward but resulted with similar model deficiencies of not predicting a strong middepth halocline.

[42] *Canuto et al.* [2001] (hereinafter referred to as CA) derive a set of stability functions that consider more terms for the pressure-strain correlations than used by KC. The CA stability functions allow for mixing to continue while approaching gradient Richardson numbers close to unity, while the KC functions fall to zero near a Richardson number of 0.21 [*Burchard and Bolding*, 2001]. A simulation with the CA stability functions resulted in overmixing compared to the observed data. The top-bottom salinity difference is fairly consistent with the KC results but the onset of stratification is delayed (on the order of 1 day on a

fortnightly timescale) and salt intruded too far into the estuary by up to 10 km.

[43] Grid resolution was also considered for model sensitivity. Increasing the number of vertical sigma levels produced results consistent with those presented here. Thus a further increase in vertical resolution was not warranted. Increased lateral resolution may lead to better resolution of the lateral shear, but will most likely not increase the ability to better resolve the vertical scalar transport.

5. Discussion

[44] For simulations of a particular estuary, the proper prescription of boundary conditions is critical. Boundaries include the free surface, the bottom closed surface, and open lateral boundaries. The free surface boundary requires scalar fluxes (we neglected a surface heat flux boundary because the density is affected more by variations in salinity than temperature) and surface wind stresses (which we also neglected) that can provide increased mixing in the near surface layer. The bottom surface requires a drag coefficient that can vary spatially and temporally. Our simulations maintained a constant value estimated from a momentum balance from previous efforts.

[45] Open lateral boundaries require prescriptions for both momentum and scalars. Momentum balances can be obtained from observations of river flows and tidal elevations. Scalar quantities along an open boundary are critical and remain a challenge to modelers because they involve processes beyond the model domain. In some estuaries, for example, the response of the river plume on the continental shelf to changes in freshwater flow or wind conditions on the shelf (upwelling or downwelling) may be important. In

Table 1. Predictive Skill of Model Parameters

Parameter	Skill (Equation (5))
Sea level	0.85–0.95
Depth-averaged velocity	0.92
Salinity	0.85
Vertical velocity profiles	0.89
Vertical salinity profiles	0.77
Salt intrusion length	0.87
Longitudinal salinity gradient	0.82
Estuarine circulation	
Near-bottom	0.78
Near-surface	0.68
Barotropic transport	0.91
Salt flux	0.91

our case, it was important to parameterize the response of the salinity field in New York Harbor to changes in freshwater flow in order to increase the skill of the numerical predictions.

[46] Skill for the different model results are listed in Table 1. The model has skill greater than 0.85 in predicting barotropic quantities of sea level, depth-averaged velocity and barotropic transport (flux of water). This skill is highest in the lower reach of the estuary where the study was focused. The skill could be increased in the upper reach of the estuary with enhanced grid resolution and accurate placement of along-estuary inflows.

[47] The model is weakest in prediction of vertical profiles of salinity (skill = 0.77), especially during neap tides when stratification is strongest. The top-bottom salinity difference is captured well but the model does not simulate as strong of a pycnocline in the vertical structure as compared to observations. This deficiency leads to a reduced skill in the longitudinal salinity gradient and the estuarine circulation. The total salt flux has a strong agreement between model and data (skill = 0.91) but has the greatest discrepancy during the neap tide on day 125.

[48] Simulations using the two equation turbulence closure models of k-kl, k-ε, and k-ω demonstrate that all three methods are consistent in their predictions of the velocity and salt transport. Deficiencies of all three closures are incorrect vertical structure of the salt stratification and reduced vertical penetration by the bottom boundary layer during spring tides. Slight variations exist between the models. These results suggest that perhaps the models underestimate the vertical flux of turbulent kinetic energy from the boundary to the interior. Also, there may be mixing processes that are not parameterized by the model, such as wetting/drying (which is typically not important in the lower Hudson River) and mixing in the upper water column perhaps due to winds or lateral boundary layers.

6. Summary and Conclusions

[49] Numerical simulations of estuarine stratification have evolved from prescriptive models to dynamically active models that solve momentum equations with varying levels of turbulence closures. In this paper we demonstrate the following.

[50] 1. A full three dimensional model with a two equation turbulence closure can predict the temporal and spatial behavior of the evolution of momentum and salt

scalar transport in an estuary with predictive skills that vary from 0.68 to 0.95. Particularly notable is the skill of simulating stratification and salt flux across a broad range of forcing conditions.

[51] 2. Proper prescription of boundary conditions is essential to satisfy scalar and momentum fluxes across the boundaries. The boundary condition for bottom stress and the open boundary condition for salinity are especially crucial for increased model skill.

[52] 3. A fully three dimensional numerical model is required that treats the salinity gradient as a dependent variable and couples the evolution of the velocity and density fields through a turbulence closure method to accurately simulate the stratification and momentum in an estuary. Results comparing the two equation turbulence closure models of k-kl, k-ε, and k-ω indicate that all three methods are consistent in their predictions of the velocity and salt transport. Deficiencies of all three closures are incorrect vertical structure of the salt stratification and reduced vertical penetration by the bottom boundary layer during spring tides.

[53] In summary, the model provides a valuable tool to provide the spatial and temporal resolution of the velocity and scalar fields not accessible by observations alone. Observations are required to assess the performance of the model and to evaluate turbulence closure models. Future model applications to the Hudson should model the salinity in New York Harbor (south of the Battery) or require observations of salinity at the open boundary. More detailed observations are required to guide improvements in the turbulence closures and the proper parameterization of bottom stress.

References

Abood, K. A. (1974), Circulation in the Hudson estuary, *Ann. N. Y. Acad. Sci.*, *250*, 39–111.

Blumberg, A. F., B. Galperin, and D. J. O'Connor (1992), Modeling vertical structure of open-channel flows, *J. Hydraul. Eng.*, *118*, 1119–1134.

Bowen, M. M., and W. R. Geyer (2003), Salt transport and the time-dependent salt balance of a partially stratified estuary, *J. Geophys. Res.*, *108*(C5), 3158, doi:10.1029/2001JC001231.

Burchard, H. (2001), On the q^2l equation by Mellor and Yamada (1982): Notes and correspondence, *J. Phys. Oceanogr.*, *31*, 1377–1387.

Burchard, H., and K. Bolding (2001), Comparative analysis of four second-moment turbulence closure models for the oceanic mixed layer, *J. Phys. Oceanogr.*, *31*, 1943–1968.

Burchard, H., O. Petersen, and T. P. Rippeth (1998), Comparing the performance of the Mellor-Yamada and the k-ε two-equation turbulence models, *J. Geophys. Res.*, *103*, 10,543–10,554.

Canuto, V. M., A. Howard, Y. Cheng, and M. S. Dubovikov (2001), Ocean turbulence I: One-point closure model. Momentum and heat vertical diffusivities, *J. Phys. Oceanogr.*, *31*, 1413–1426.

Chatwin, P. C. (1976), Some remarks on the maintenance of the salinity distribution in estuaries, *Estuarine Coastal Mar. Sci.*, *4*, 555–566.

de Vries, M. P., and L. A. Weiss (2001), Salt-front movement in the Hudson River estuary, New York—Simulations by one-dimensional flow and solute-transport models, *U.S. Geol. Surv. Water Resour. Invest. Rep.*, *99-4024*, 69 pp.

Ezer, T., H. G. Arango, and A. F. Shchepetkin (2002), Developments in terrain-following ocean models: Intercomparisons of numerical aspects, *Ocean Modell.*, *4*, 249–267.

Geyer, W. R., and D. M. Farmer (1989), Tide-induced variation of the dynamics of a salt wedge estuary, *J. Phys. Oceanogr.*, 19, 1060–1072.

Geyer, W. R., J. H. Trowbridge, and M. M. Bowen (2000), The dynamics of a partially mixed estuary, *J. Phys. Oceanogr.*, 30, 2035–2048.

Haas, L. W. (1977), The effect of the spring-neap tidal cycle on the vertical salinity structure of the James, York, and Rappahannock rivers, *Estuarine Coastal Mar. Sci.*, 5, 485–496.

Haidvogel, D. B., H. G. Arango, K. Hedstrom, A. Beckmann, P. Malanotte-Rizzoli, and A. F. Shchepetkin (2000), Model evaluation experiments in the North Atlantic Basin: Simulations in nonlinear terrain-following coordinates, *Dyn. Atmos. Oceans*, 32, 239–281.

Hansen, D. V., and M. Rattray (1965), Gravitational circulation in straits and estuaries, *J. Mar. Res.*, 23, 104–122.

Hetland, R. D., and W. R. Geyer (2005), An idealized study of the structure of long, partially mixed estuaries, *J. Phys. Oceanogr.*, in press.

Jay, D. A., and J. D. Musiak (1996), Internal tidal asymmetry in channel flows: Origins and consequences, in *Mixing in Estuaries and Coastal Seas*, *Coastal Estuarine Stud.*, vol. 50, edited by C. Pattiaratchi, pp. 211–249, AGU, Washington, D. C.

Kantha, L. H., and C. A. Clayson (1994), An improved mixed layer model for geophysical applications, *J. Geophys. Res.*, 99, 25,235–25,266.

Kranenburg, C. (1986), A timescale for long term salt intrusion in well-mixed estuaries, *J. Phys. Oceanogr.*, 16, 1329–1331.

MacCready, P. (1999), Estuarine adjustment to changes in river flow and tidal mixing, *J. Phys. Oceanogr.*, 29, 708–726.

Mellor, G. L., and T. Yamada (1982), Development of a turbulence closure model for geophysical fluid problems, *Rev. Geophys.*, 20, 851–875.

Monismith, S. G., and D. A. Fong (1996), A simple model of mixing in a stratified tidal flows, *J. Geophys. Res.*, 101, 28,583–28,595.

Monismith, S. G., J. R. Burau, and M. T. Stacey (1996), Stratification dynamics and gravitational circulation in northern San Francisco Bay, in *San Francisco Bay: The Ecosystem*, edited by T. Hollibaugh, pp. 123–153, Am. Assoc. for the Advance. of Sci., Washington, D. C.

North, E. W., S.-Y. Chao, L. P. Sanford, and R. R. Hood (2004), The influence of wind and river pulses on an estuarine turbidity maximum: Numerical studies and field observations in Chesapeake Bay, *Estuaries*, 27, 132–146.

Nunes Vaz, R. A., and J. H. Simpson (1994), Turbulence closure modeling of estuarine stratification, *J. Geophys. Res.*, 99, 16,143–16,160.

Nunes Vaz, R. A., G. W. Lenon, and J. R. de Silva Samarasinghe (1989), The negative role of turbulence in estuarine mass transport, *Estuarine Coastal Shelf Sci.*, 28, 361–377.

Prandle, D. (2004), Saline intrusion in partially mixed estuaries, *Estuarine Coastal Shelf Sci.*, 59, 385–397.

Rodi, W. (1984), Turbulence models and their application in hydraulics—A state of the art review, technical report, Int. Assoc. for Hydraul. Res., Delft, Netherlands.

Sharples, J., and J. H. Simpson (1993), Periodic frontogenesis in a region of freshwater influences, *Estuaries*, 16, 74–82.

Shchepetkin, A. F., and J. C. McWilliams (2003), A method for computing horizontal pressure-gradient force in an oceanic model with a nonaligned vertical coordinate, *J. Geophys. Res.*, 108(C3), 3090, doi:10.1029/2001JC001047.

Shchepetkin, A. F., and J. C. McWilliams (2005), The Regional Ocean Modeling System: A split-explicit, free-surface, topography-following coordinates ocean model, *Ocean Modell.*, 9, 347–404, doi:10.1016/j.ocemod.2004.08.002.

Simpson, J. H., and J. Sharples (1991), Dynamically-active models in the prediction of estuarine stratification, in *Dynamics and Exchanges in Estuaries and the Coastal Zone*, edited by D. Prandle, pp. 101–113, Springer, New York.

Simpson, J. H., J. Brown, J. Matthews, and G. Allen (1990), Tidal straining, density currents, and stirring in the control of estuarine stratification, *Estuaries*, 13, 125–132.

Simpson, J. H., J. Sharples, and T. P. Rippeth (1991), A prescriptive model of stratification induced by freshwater runoff, *Estuarine Coastal Shelf Sci.*, 33, 23–35.

Stacey, M. T. (1996), Turbulent mixing and residual circulation in a partially stratified estuary, Ph.D. thesis, 209 pp., Dep. of Civ. Eng., Stanford Univ., Calif.

Stenström, P. (2004), Hydraulics and mixing in the Hudson River estuary: A numerical model study of the tidal variations during neap tide conditions, *J. Geophys. Res.*, 109, C04019, doi:10.1029/2003JC001954.

Umlauf, L., and H. Burchard (2003), A generic length-scale equation for geophysical turbulence models, *J. Mar. Res.*, 61, 235–265.

Umlauf, L., H. Burchard, and K. Hutter (2003), Extending the k-omega turbulence model towards oceanic applications, *Ocean Modell.*, 5, 195–218.

Warner, J. C., C. R. Sherwood, H. G. Arango, and R. P. Signell (2005), Performance of four turbulence closure models implemented using a generic length scale method, *Ocean Modell.*, 8, 81–113.

Wells, A. W., and J. R. Young (1992), Long-term variability and predictability of Hudson River physical and chemical characteristics, in *Estuarine Research in the 1980s*, edited by C. Lavett Smith, pp. 29–58, State Univ. of N. Y. Press, Albany.

Wilcox, D. C. (1988), Reassessment of the scale determining equation for advance turbulence models, *AIAA J.*, 26, 1299–1310.

Wilcox, D. C. (1998), *Turbulence Modeling for CFD*, 540 pp., DCW Indust., La Cañada, Calif.

Wilmott, C. J. (1981), On the validation of models, *Phys. Geogr.*, 2, 184–194.

Zhou, M. (1998), Influence of bottom stress on the two-layer flow induced by gravity currents in estuaries, *Estuarine Coastal Shelf Sci.*, 46, 811–825.

————————

W. R. Geyer, Applied Ocean Physics and Engineering, Woods Hole Oceanographic Institution, MS 12, Woods Hole, MA 02543, USA. (rgeyer@whoi.edu)

J. A. Lerczak, Department of Physical Oceanography, Woods Hole Oceanographic Institution, MS 21, Woods Hole, MA 02543, USA. (jlerczak@whoi.edu)

J. C. Warner, U.S. Geological Survey, 384 Woods Hole Road, Woods Hole, MA 02543, USA. (jcwarner@usgs.gov)